



1  
2  
3  
4  
5  
6  
7  
8  
9  
10  
11  
12  
13  
14  
15  
16  
17  
18  
19  
20  
21  
22  
23  
24  
25  
26  
27

## Ground-based Temperature and Humidity Profiling: Combining Active and Passive Remote Sensors

David D. Turner<sup>1</sup> and Ulrich Löhnert<sup>2</sup>

<sup>1</sup> NOAA / OAR / Global Systems Laboratory

<sup>2</sup> University of Cologne / Institute of Geophysics and Meteorology

Submitted 31 August 2020

*Special Issue for the 11<sup>th</sup> International Symposium on Tropospheric Profiling in Atmospheric Measurement Technology*

Corresponding Author:

Dr. David Turner  
NOAA Global Systems Laboratory  
325 Broadway, Boulder, CO 80305  
Voice: +1-303-497-6097  
Email: dave.turner@noaa.gov



## 28 Abstract

29

30 Thermodynamic profiles in the planetary boundary layer (PBL) are important observations for a  
31 range of atmospheric research and operational needs. These profiles can be retrieved from  
32 passively sensed spectral infrared (IR) or microwave (MW) radiance observations, or can be  
33 more directly measured by active remote sensors such as water vapor differential absorption  
34 lidars (DIALs). This paper explores the synergy of combining ground-based IR, MW, and DIAL  
35 observations using an optimal estimation retrieval framework, quantifying the reduction in the  
36 uncertainty in the retrieved profiles and the increase in information content as additional  
37 observations are added to IR-only and MW-only retrievals.

38

39 This study uses ground-based observations collected during the Perdigao field campaign in  
40 central Portugal in 2017 and during the DIAL demonstration campaign at the Atmospheric  
41 Radiation Measurement Southern Great Plains site in 2017. The results show that the  
42 information content in both temperature and water vapor is higher for IR instrument relative to  
43 the MW instrument (thereby resulting in smaller uncertainties), and that the combined IR+MW  
44 retrieval is very similar to the IR-only retrieval below 1.5 km. However, including the partial  
45 profile of water vapor observed by the DIAL increases the information content in the combined  
46 IR+DIAL and MW+DIAL water vapor retrievals substantially, with the exact impact vertically  
47 depending on the characteristics of the DIAL instrument itself. Furthermore, there is slight  
48 increase in the information content in the retrieved temperature profile using the IR+DIAL  
49 relative to the IR-only; this was not observed in the MW+DIAL retrieval.

50



## 51 1. Introduction

52 High temporal resolution thermodynamic profiles in the planetary boundary layer (PBL)  
53 are needed for a wide range of research and operational weather forecasting needs  
54 (Wulfmeyer et al. 2015). For example, the vertical distribution of water vapor and temperature  
55 changes markedly over the diurnal cycle, the passage of synoptic features such as frontal  
56 boundaries and dry lines can cause very rapid changes in the thermodynamic structure of the  
57 PBL, and the evolution of convective weather with evaporation-driven cold pools impacts both  
58 the temperature and humidity profiles and feeds back on the storm's evolution. Indeed, a large  
59 number of groups have called for improvements in the thermodynamic profiling in the PBL, and  
60 the establishment of ground-based networks to provide these datasets to the atmospheric  
61 science community (e.g., Dabberdt et al. 2005; NRC 2009).

62 Progress is being made, albeit perhaps slowly. There are a large number of case studies  
63 using PBL thermodynamic profiling systems to gain insight into how the convective properties  
64 of atmosphere changes (e.g., Feltz et al. 2003; Cimini et al. 2015; Bluestein et al. 2017; Toms et  
65 al. 2017; Mueller et al. 2017), analyses of long-time series to show the capability of these  
66 systems (Löhnert and Maier 2012; Wagner et al. 2008), and utility for improving short-term  
67 nowcasts and forecasts (e.g., Cimini 2011; Caumont et al. 2016; Hu et al. 2019; Coniglio 2019).

68 In Europe, there are a large number of microwave radiometers that are being  
69 characterized and assimilated (experimentally) into numerical weather prediction models  
70 (Cimini et al. 2018; De Angelis et al. 2017). Activities in the US have focused primarily on field  
71 campaigns, and the Plains Elevated Convection at Night (PECAN; Geerts et al. 2017) in  
72 particular, which deployed a small network of 6 infrared spectrometers in the central US. The  
73 PECAN observations are being used to study a range of atmospheric phenomena both  
74 observationally (e.g., Gasmick et al. 2018; Loveless et al. 2019) and via use in numerical weather  
75 prediction models (Johnson et al. 2018; Degelia et al. 2019).

76 However, these different ground-based remote sensors have generally not been  
77 collocated which makes evaluating the relative differences in the information content of the  
78 observations difficult. This paper takes advantage of two field campaigns where multiple  
79 ground-based remote sensing systems were collocated to evaluate the relative strengths and  
80 weaknesses of these different observations for thermodynamic profiling in the PBL. The two  
81 campaigns are Perdigao, which occurred in central Portugal in May-June of 2017 (Fernando et  
82 al. 2019), and a campaign at the ARM Southern Great Plains site (Sisterson et al. 2016) in May-  
83 June 2017 to compare a newly developed broadband differential absorption lidar for water  
84 vapor profiling with other instruments (Newsom et al. 2020).

## 85 2. Instruments

86 While there are many different instruments that could be included in this analysis, we  
87 will focus on four instruments that have been demonstrated to run operationally in unattended  
88 modes for weeks or longer, and either already are or will likely soon become commercially  
89 available. Two of these instruments are passive remote sensors (i.e., they do not transmit  
90 electromagnetic energy to the atmosphere) while two are active remote sensors.



## 91        2.1. Microwave radiometer

92            One type of passive thermodynamic profiler is a microwave radiometer (MWR). MWRs  
93 used for thermodynamic profiling typically have multiple channels along the high frequency  
94 side of the 22.2 GHz water vapor absorption line (i.e., from 22.2 to 31 GHz) and on the low  
95 frequency side of the 60 GHz oxygen absorption complex (i.e., from 51 to 60 GHz). Height  
96 dependent pressure broadening of the water vapor line allows the retrieval of a coarsely  
97 resolved water vapor profile, whereas temperature profile information is obtained from the  
98 frequency dependent optical depth. Generally speaking, the more transparent frequencies  
99 provide information through a deeper portion of the atmosphere and the optically thick  
100 channels provide information closer to the MWR. Oxygen is well mixed in the atmosphere and  
101 its concentration is known, thus the downwelling radiance observed in the channels that are  
102 primarily sensitive to oxygen can be used to infer the temperature profile. Water vapor  
103 concentration profiles can be determined from the channels that have sensitivity to water  
104 vapor after the temperature profile is known. However, there is some level of absorption due  
105 to oxygen in the 22-31 GHz range and water vapor in the 51-60 GHz range, so retrieval methods  
106 need to account for this ‘cross-talk’, and provide some estimate of the correlated errors in the  
107 retrieved profiles.

108            For this study, we used a 14-channel Humidity and Temperature Profiling (HATPRO)  
109 microwave radiometer (Rose et al. 2005). This is a fourth-generation system, which is part of  
110 the Collaborative Lower Atmospheric Mobile Profiling System (CLAMPS; Wagner et al. 2019).  
111 The instrument specifications are given in Table 1. The radiometric uncertainty in these  
112 observations were determined via a time-series analysis of the observed brightness  
113 temperatures when the atmosphere could be assumed to be quasi-stationary. These values are  
114 provided in Table 1. These radiometric uncertainties are assumed to be uncorrelated between  
115 the different channels.

## 116        2.2. AERI

117            The second passive remote sensor studied here is the Atmospheric Emitted Radiance  
118 Interferometer (AERI). The AERI is a Fourier transform spectrometer designed to measure  
119 infrared radiation emitted by the atmosphere between 3.3 and 19  $\mu\text{m}$  in wavelength (3000 to  
120 520  $\text{cm}^{-1}$ ) with a spectral resolution of 0.5  $\text{cm}^{-1}$ . The AERI was designed specifically for the  
121 Department of Energy’s Atmospheric Radiation Measurement (ARM) program (Turner et al.  
122 2016a; Knuteson et al. 2004 a,b). Its specifications can also be found in Table 1.

123            The radiometric uncertainty in the AERI observations is derived from the imaginary  
124 component of the AERI’s calibration equation (Revercomb et al. 1988), and thus the noise  
125 spectrum can be derived for each sky observation period. Turner and Blumberg (2019) have  
126 demonstrated that the radiometric noise in the AERI observations is spectrally uncorrelated.  
127

## 128        2.3. NCAR water vapor DIAL

129            Water vapor differential absorption lidar (DIAL) work by transmitting pulsed laser energy at  
130 two wavelengths, one of which is selected to have markedly higher water vapor absorption  
131 than the other. These two frequencies are typically referred to as the on-line and off-line



132 frequencies. If the two wavelengths are spectrally close to each other (e.g., within a nm in  
133 wavelength), then many of the terms that describe the ratio of the strength of the  
134 backscattered signals cancel out. The ratio of the on- to off-line return signals is directly related  
135 to the water vapor concentration profile.

136 The National Center for Atmospheric Research (NCAR) has developed a micropulse water  
137 vapor DIAL. The approach used by this lidar is the so-called “narrowband DIAL” approach  
138 wherein the laser emits monochromatic pulses of energy. Thus, because the characteristics of  
139 the absorption line are well known, the method is self-calibrating and no external calibration  
140 source is needed. Narrowband DIAL systems require extremely high spectral purity in the  
141 outgoing laser, as subtle changes in the wavelength (especially for the on-line channel) even for  
142 a small number of laser pulses in the averaging window can introduce biases in the derived  
143 water vapor profile because the incorrect absorption cross-section is used in the derivation.

144 The laser in the NCAR DIAL, henceforth called the nDIAL, emits low pulse energies at high  
145 pulse repetition rate (Spuler et al 2015). The outgoing laser beam is expanded by a portion of  
146 the primary telescope, which makes the lidar system eye-safe. The nDIAL system has its origins  
147 at Montana State University (MSU), wherein commercially available laser diodes developed for  
148 telecommunications were used as the laser source (Nehrir et al. 2012), and MSU continues to  
149 collaborate with NCAR to advance the nDIAL technology. A single photon counting detector is  
150 used to detect the backscattered signals in both the on-line and off-line channels. High  
151 transmission, narrowband interference filters are used to reject energy (e.g., solar background)  
152 outside the desired frequency range of the desired signals. The technical details of this system  
153 are provided in Table 1.

154 The signal-to-noise ratio (SNR) in DIAL systems is strongly dependent upon the strength of  
155 the backscattering signal as a function of range. Aerosol particles provide an efficient scattering  
156 source, and because aerosol concentration decreases markedly above the top of the PBL, the  
157 SNR also drops sharply above this level. However, the actual range wherein the lidar makes  
158 good water vapor measurements is a function of the pulse energy, the efficiency of the  
159 detector system (e.g., size of the telescope, transmission of the detection optics, sensitivity of  
160 the detector), and the vertical profiles of both the aerosol and water vapor concentrations. For  
161 this study, the backscattered photon data were coadded for 1-minute before deriving the water  
162 vapor profile.

163 Virtually all lidar systems have difficulties accurately measuring atmospheric properties  
164 close to the lidar itself. Ultimately, this is due to a mismatch between the outgoing laser beam  
165 and the detector and leads to a systematic error that varies with height. This systematic error  
166 reduces to zero at some range, and the region where the error is nonzero is referred to as the  
167 “overlap” region. For many lidar systems, an empirically determined correction can be applied  
168 to reduce the maximum range of the non-zero overlap error. For the current version of the  
169 nDIAL, approximately the lowest 500 m suffers from a varying overlap correction (S. Spuler,  
170 personal communication), and thus is not used in this analysis.

171 The uncertainty in the nDIAL observations is directly calculated by assuming that the  
172 detected backscatter signal follows a Poisson distribution, and propagating the uncertainty in  
173 the backscatter profile through the DIAL equation. A similar approach was used for the SGP  
174 Raman lidar, and the noise estimate derived from Poisson statistics agrees with that derived  
175 using an autocovariance analysis (Turner et al. 2014).



176 The nDIAL has been deployed in a number of different field campaigns. In particular, the  
177 water vapor profile observed by the nDIAL have been compared to water vapor profiles  
178 measured by radiosondes and independently retrieved from collocated AERI and MWR systems  
179 (Weckwerth et al. 2016). These comparisons demonstrate that the nDIAL agrees well with these  
180 other sensors (e.g., the bias error relative to radiosondes is less than  $0.3 \text{ g/m}^3$ ) and has no  
181 significant day vs. night differences in sensitivity (e.g. due to solar background). In 2018, NCAR  
182 constructed 4 additional units (bringing the total number of nDIAL systems to five), which were  
183 deployed in a network configuration at the Department of Energy's Atmospheric Radiation  
184 Measurement (ARM) Southern Great Plains site (SGP, Sisterson et al. 2016) from April through  
185 July 2019.

#### 187 *2.4. Vaisala water vapor DIAL*

188 Vaisala is also developing a micropulse water vapor DIAL (henceforth called the vDIAL). This  
189 lidar system is based upon the CL51 ceilometer design; this ceilometer is used operationally  
190 around the world. Unlike the nDIAL, the vDIAL transmits a spectrally broad pulse of laser  
191 energy that encompasses several water vapor absorption lines ("on-line channel") and in a  
192 nearby spectral window with no absorption lines ("off-line"). This approach is less technically  
193 demanding on the laser specifications (e.g., the requirement for high spectral purity is much  
194 smaller), but the tradeoff is that the measurement is no longer self-calibrating (Newsom et al.  
195 2020). For this particular broadband DIAL implementation, the reference measurement is a  
196 well-calibrated surface level in-situ sensor integrated into the DIAL, and measurements from  
197 this sensor are used in an iterative retrieval approach to derive the water vapor profile  
198 (Newsom et al. 2020).

199 The vDIAL actually consists of two independent broadband DIAL systems integrated  
200 together. The first system has a wide field-of-view, thereby resulting in a very small overlap  
201 region and allowing the lidar to profile water vapor down to 50 m above ground level (AGL).  
202 However, this wide field-of-view results in additional solar background photons and the SNR  
203 decreases very rapidly with range. The second system has a much narrower field of view, which  
204 results in a deeper overlap region but also enables the lidar to profile water vapor much higher.  
205 Cross-talk between the two independent systems is eliminated by operating one system for 5-s,  
206 and then operating the other for the next 5-s. The water vapor profiles are derived  
207 independently for the wide and narrow field-of-view systems, and then they are merged  
208 linearly between 300 and 400 m. Additional details on this system are provided in Newsom et  
209 al. (2020).

210 The vDIAL system uses analog detection, and thus the uncertainties in the backscatter do  
211 not follow a Poisson distribution like in the nDIAL. Instead, the uncertainties in the vDIAL water  
212 vapor profile are estimated by deriving water vapor profiles every 2-minutes, and computing  
213 the standard deviation from these data at each height across a 20-minute window to provide  
214 the uncertainty in the standard 20-min average water vapor profile.

215 The vDIAL system was deployed to the ARM SGP in May-June 2017, where it was compared  
216 against water vapor profiles observed by the ARM Raman lidar (Turner et al. 2016b; Turner and  
217 Goldsmith 1999), radiosondes, and retrieved from the AERI.



### 218 3. Retrieval algorithm

219 Passive spectral radiometers, such as the MWRs and AERIs, measure radiance, and  
220 thermodynamic profiles must be retrieved from these observations. However, this is an ill-  
221 posed problem, as there could exist multiple solutions (e.g., different thermodynamic profiles)  
222 that would yield the observed radiance. Thus, the retrieval algorithm must incorporate  
223 additional information to constrain the solution to a potentially valid solution. Here, we have  
224 elected to use the optimal estimation approach (Rodgers 2000; Maahn et al. 2020), which is a  
225 1-dimensional variational method. We have modified the AERIOe optimal estimation retrieval  
226 algorithm (Turner and Löhnert 2014) to use AERI and/or MWR data, together with *a priori*  
227 dataset that specifies how temperature and humidity covary with height, as input. This  
228 algorithm has already been modified to include additional observations, such as water vapor  
229 lidars (Turner and Blumberg 2019), and thus in these cases the retrieval is finding the  
230 temperature and humidity profiles that satisfies both the observed radiance and the (partial)  
231 profile of water vapor observed by the DIAL simultaneously.

232 We desire to retrieve the thermodynamic profile  $X$  (i.e., both the temperature and  
233 humidity profile, so  $X = \left[ [T_1, T_2, \dots, T_p]^T, [q_1, q_2, \dots, q_p]^T \right]$  where  $T_i$  and  $q_i$  are the temperature  
234 and water vapor mixing ratio in the  $i^{\text{th}}$  vertical bin. We will refer to  $X_n$  as the state vector on  
235 the  $n^{\text{th}}$  iteration. The observations from the AERI, MWR, and DIALs will form the observation  
236 vector  $Y$ . A forward model  $F$  is used to compute a pseudo observation  $F(X)$ , which is then  
237 compared with  $Y$ . If they disagree, then the state vector is modified to provide a new estimate  
238 ( $X_{n+1}$ ) following

$$239 \quad X_{n+1} = X_a + (\gamma S_a^{-1} + K_n^T S_\epsilon^{-1} K_n)^{-1} K_n^T S_\epsilon^{-1} (Y - F(X_n) + K_n(X_n - X_a)) \quad (\text{Eq 1})$$

240 where  $K$  is the Jacobian of  $F$ ,  $X_a$  is the mean *a priori*, and  $S_a$  is the covariance matrix of the *a*  
241 *priori* dataset (see Section 3.2).  $S_\epsilon$  denotes the combined forward model and observation error  
242 covariance matrix. The observation error for the single instruments is considered as described  
243 in the subsection of Section 2 and the forward model uncertainty is discussed in Section 3.1.  
244 The superscripts  $^T$  and  $^{-1}$  denote matrix transpose and matrix inverse, respectively. Because  $F$   
245 is moderately non-linear in  $X$ , optimal estimation is formulated as an iterative method, where the  
246 subscript  $n$  indicates the iteration number; for our studies, we typically start with  $X_0 = X_a$ . The  
247 scalar  $\gamma$  is used to stabilize the retrieval when  $n$  is small to improve the convergence rate and  
248 decreases to unity as  $n$  increases; the description on how  $\gamma$  is used is explained in Turner and  
249 Löhnert (2014). Note that due to the non-linearity of the forward models applied for the  
250 microwave and infrared radiative transfer, the Jacobians are required to be recomputed for  
251 each iteration. We continue to iterate Eq 1 until

$$252 \quad (F(X_{n+1}) - F(X_n))^T (K_n S_a K_n^T + S_\epsilon)^{-1} (F(X_{n+1}) - F(X_n)) \ll m \quad (\text{Eq 2})$$

253 where  $m$  is the dimension of  $Y$ .



### 254 3.1. Forward models

255 As shown by Eq 1, a forward model is needed to transform the current state vector  $X_n$  into  
256 the observational domain so it can then be compared to the observation vector  $Y$ . In this  
257 study, four different forward models are used (one for each instrument).

258 For the passive radiometers, the forward models are line-by-line radiative transfer models.  
259 The monochromatic MonoRTM radiative transfer model (Clough et al. 2005; Payne et al. 2011)  
260 is used to simulate MWR observations, and the line-by-line radiative transfer model LBLRTM  
261 (Clough et al. 1995; Mlawer and Turner 2016) is used to simulate the AERI. In the latter, the  
262 monochromatic spectra are convolved with a tophat function in the time domain and then  
263 transformed to the spectral domain via a Fourier transform; this applies the AERI's lineshape  
264 function to the calculation. The vertical grid used in these calculations is specified by the *a*  
265 *priori* data. The pressure profile is computed from the temperature and humidity data from the  
266 current state vector using the hypsometric equation. The spectral regions used in the retrieval  
267 are given in Table 1. In the infrared, many trace gases have absorption bands, and while the  
268 spectral regions used in the retrieval are primarily sensitive to water vapor and carbon dioxide  
269 (where the latter provides the sensitivity to temperature), there are minor contributions to the  
270 downwelling radiance by other gases. We utilize the US Standard Atmosphere to provide  
271 profiles of these other trace gases for this study, but our results are insensitive to this choice.

272 To incorporate the DIAL data into the Eq 1, a forward model is needed for each lidar also.  
273 The purest forward model would simulate the profiles of backscatter energy that would be  
274 observed in both the on- and off-line channels for a given water vapor profile. We have elected  
275 to use the derived water vapor concentration from each lidar in the observation vector. This  
276 results in a trivial forward model for each lidar: essentially, the forward model just converts  
277 water vapor mixing ratio to water vapor number concentration for the nDIAL. The output of  
278 the vDIAL is water vapor mixing ratio, so that forward model is just the unity function.

### 279 3.2. The *a priori* dataset

280 There has been only one campaign that had an AERI, HATPRO, and water vapor DIAL  
281 collocated with each other: the Perdigao campaign that was held in Portugal from 1 May to 15  
282 June 2017 (Fernando et al. 2019). We specified a 48-level vertical grid for the retrievals,  
283 starting at 0 m above ground level (AGL), the next level at 10 m AGL, and each subsequent  
284 height bin is 10% thicker than the previous one. Although ~150 radiosondes were launched  
285 during Perdigao, these are not enough to accurately compute the level-to-level covariance for  
286 the 96-element state vector (i.e.,  $X$  has 48 levels for temperature, and 48 for water vapor).  
287 Therefore, we used 1571 radiosondes launched in the months of April, May, June, and July over  
288 the last decade by the Portuguese weather service at Lisbon to compute  $X_a$  and  $S_a$ . This *a*  
289 *priori* information was used in all of the retrievals shown here.

290 The vDIAL was not part of the Perdigao deployment, so we are using AERI and vDIAL data  
291 collected between 15 May to 12 June 2017 at the SGP site instead. Both the Perdigao and SGP  
292 datasets used here were collected in the spring, but the SGP climatology is different than that in  
293 Portugal necessitating the use of a different *a priori* dataset. We have used over 2000  
294 radiosondes launched at the SGP during the months of April, May, and June over the past  
295 decade to derive the *a priori* information for this site.





### 296 3.3. Characterizing the information content in the retrieved profile

297 One advantage of the optimal estimation framework is that the uncertainties in the  
298 retrieval, which includes contributions from both the uncertainties in the observations and *a*  
299 *priori* as well as the sensitivity of the forward model, is a direct output of the framework. If the  
300 “optimal” solution is  $X_{op}$ , which is the solution after both  $\gamma = 1$  and Eq 2 indicates that the  
301 solution has converged after  $nc$  iterations, then the covariance of the optimal solution is given  
302 by

$$303 S_{op} = (S_a^{-1} + K_{nc}^T S_\epsilon^{-1} K_{nc})^{-1} \quad (\text{Eq 3})$$

304 We will look at the square root of the diagonal elements of  $S_{op}$  to quantify how the  $1-\sigma$   
305 uncertainties of the retrieved profiles change as different instrument combinations are used in  
306 the observation vector.

307 A second advantage of this method is that the averaging kernel  $A$  provides a direct estimate  
308 of the sensitivity of the retrieved profile at each height to perturbations at that height. This  
309 matrix is computed as

$$310 A = (S_a^{-1} + K_{nc}^T S_\epsilon^{-1} K_{nc})^{-1} K_{nc}^T S_\epsilon^{-1} K_{nc} = I - S_{op} S_a^{-1} \quad (\text{Eq 4})$$

311 The diagonal components of  $A$  provides the degrees of freedom for signal (DFS; Rodgers 2000)  
312 for each height in the retrieved profile. If the observations had very high information content  
313 at each level of the retrieved profile, then the diagonal elements of  $S_{op}$  would be small relative  
314 to the diagonal elements of the *a priori*, and thus the trace of  $A$  would approach the dimension  
315 of  $X$ . The total DFS, which is equal to the trace of  $A$ , provides a metric for how many  
316 independent pieces of information exist in the observation.

317 For this study, we recognize that the matrices  $A$ ,  $S_{op}$ , and  $S_a$  really have four equal sized  
318 quadrants that correspond to

$$319 \begin{bmatrix} (T, T) & (T, q) \\ (q, T) & (q, q) \end{bmatrix}$$

320 We will look at the portions of  $A$  and  $S_{op}$  that correspond to  $(T, T)$  and  $(q, q)$  independently.  
321 Furthermore, as we will see, the DFS is typically much smaller than unity, so we will look at the  
322 profile of the cumulative DFS (cDFS), as this allows us to quickly determine how many  
323 independent levels are below some specified height, which is advantageous when talking about  
324 where in the vertical the different instruments provide sensitivity to changes in temperature  
325 and water vapor.

326 We want to highlight that even though lidars make explicitly range resolved measurements,  
327 their information content in the derived water vapor profile is not the same as the number of  
328 range bins. The actual information content at height  $z$  depends strongly on the noise level of  
329 the observation there. Even direct derivations of water vapor from lidar signals would benefit  
330 from being cast into a retrieval framework like what we’ve specified in Eq 1 because then the *a*  
331 *priori* information could be used to constrain the derived water vapor when the instrument’s  
332 SNR decreases (e.g., Sica and Haeefe 2016).

## 333 4. Results

334 Several studies have demonstrated that ground-based thermodynamic retrievals in the PBL  
335 using only AERI observations have 2-4 times larger total DFS in both temperature and water



336 vapor than retrievals that use only microwave data (Löhnert et al. 2009; Blumberg et al. 2015;  
337 Wulfmeyer et al 2015). However, what is not known is how the information content changes  
338 when partial profiles of water vapor from a differential absorption lidar (since the DIAL  
339 observations extend only from the top of the region where full overlap is achieved to a height  
340 where its SNR becomes small) are included in a retrieval considering the synergy of AERI, MWR,  
341 and nDIAL or vDIAL. For example, does including a partial water vapor profile in the retrieval  
342 result in AERI+DIAL and MWR+DIAL having equivalent cDFS for water vapor? Does including a  
343 partial water vapor profile in a simultaneous retrieval of  $T(z)$  and  $q(z)$  (as we are doing here in  
344 Eq 1) improve the temperature profile in any way?

345 In order to answer these questions, we performed eight sets of retrievals using data from  
346 the Perdigao field campaign in Portugal (Table 2): four were using passive-only measurements  
347 (MWRz, MWRzo, AERI, and AERI+MWRz), and four included the nDIAL together with those  
348 passive measurements. “MWRz” denotes the case when only zenith-pointing MWR brightness  
349 temperature observations were used in the retrieval, whereas “MWRzo” denotes the case were  
350 both zenith and off-zenith (i.e., “oblique” elevation scans) are used. Crewell and Löhnert (2007)  
351 demonstrated that adding elevation scan observations at frequencies where the atmosphere is  
352 optically thick, and assuming horizontal homogeneity of the PBL, resulted in a marked increase  
353 in the information content and hence accuracy of the retrieved temperature profile. However,  
354 only observations made at frequencies above 55 GHz are used in these elevation scans. Even at  
355 low elevation angles, frequencies channels below 55 GHz are too transparent and thus the  
356 assumption of horizontal homogeneity fails very frequently (Crewell and Löhnert 2007).

357 As the vDIAL will soon be the first commercially available DIAL instrument for water vapor  
358 profiling (H. Winston, personal communication), a major objective is to evaluate how including  
359 this lidar dataset with passive observations changes the information content in the retrieved  
360 profiles. In addition, we show the impact of the vDIAL relative to the nDIAL on our retrievals.  
361 However, vDIAL (ARM SGP) and nDIAL (Perdigao) observations are only available at different  
362 locations with different *a priori* datasets. In order to overcome this issue, the comparisons were  
363 carried out in relation to the AERI instruments, which operated at both sites. The comparison of  
364 the AERI-only from ARM-SGP and Perdigao allows us to characterize the impact of the prior on  
365 the retrievals, since the two AERI instruments deployed in Portugal and at the SGP site have  
366 similar error characteristics (not shown). Ultimately, we have looked at the differences  
367 between the AERI-only and AERI+xDIAL retrievals (where x is either “v” or “n”) at the two sites.

#### 368 **4.1. Case study example**

369 To illustrate the differences between the various passive-only and passive+active retrievals,  
370 we selected a case during Perdigao on 15 May 2017 at 05:07 UTC. This is a clear sky event, and  
371 is representative of the retrieval quality during the entire field campaign. Figure 1 shows the  
372 retrieved temperature (panel A) and water vapor mixing ratio (WVMR, panel B), and the  
373 associated  $1-\sigma$  uncertainties of each (panels C and D, respectively) derived from the square root  
374 of the diagonal of the retrieval error covariance  $S_{op}$ . The black line in panels A and B denote  
375 the coincident radiosonde, whereas the other colors denote the different passive-only  
376 retrievals.

377 All three passive-only retrievals (MWRzo, AERI, and AERI+MWRzo) identify the surface-  
378 based inversion, although the retrievals that include the AERI capture it more accurately (Fig



379 1A). Furthermore, the retrievals that include the AERI are able to better match the radiosonde  
380 temperature observations above 1.5 km, whereas the MWRzo retrieval is showing a bias at  
381 those altitudes. None of the three retrievals are able to capture the small-scale variability in the  
382 vertical observed by the radiosonde due to the relatively coarse vertical resolution of the  
383 retrievals. The uncertainties in the MWRzo temperature retrievals are about 50% larger (or  
384 more) over the lowest 3 km relative to the AERI retrievals (Fig 1C), which agrees qualitatively  
385 with the differences to the radiosonde seen in Fig 1A.

386 The water vapor retrievals (Fig 1B) show two basic vertical patterns: the MWRzo retrieval is  
387 markedly drier than the radiosonde below 1 km, whereas the AERI and AERI+MWRzo retrieval  
388 starts dry, then becomes too wet (between 500 and 1000 m), and then becomes drier than the  
389 radiosonde above 1500 m. Interestingly, the nDIAL water vapor profile is also drier than the  
390 radiosonde below 1500 m, and agrees better with the MWRzo profile. However, the retrievals  
391 that use the AERI data have markedly smaller uncertainties than the MWRzo below 1.5 km;  
392 above that height, the uncertainty in the MWRzo is smaller than the AERI, although the  
393 AERI+MWRzo retrieval has the smallest uncertainties over the entire lowest 3 km as would be  
394 expected for a variational retrieval method.

395 Including the nDIAL data above 500 m into the retrieval, and thus finding a solution that  
396 simultaneously fits both the observed radiance and the partial WVMR profile of the DIAL within  
397 their uncertainties, yields the results shown in Fig 2. The largest impact, not surprisingly, is on  
398 the retrieved water vapor profile (Fig 2B). The inclusion of the nDIAL data forces the retrievals  
399 that also include the AERI to reduce the amount of water vapor between 500 and 1000 m  
400 (where the AERI-based retrievals were too wet in Fig 1B), which has the impact of increasing  
401 the amount of water vapor in the AERI retrievals below 500 m (Fig 2B), resulting in the  
402 AERI+nDIAL and AERI+MWRzo+nDIAL agreeing much better with the radiosonde. Between 800  
403 and 1500 m, the MWR+nDIAL retrieved profile is essentially the same as the nDIAL profile,  
404 suggesting that the MWR is not adding any significant information to the DIAL's observation.  
405 The impact of the nDIAL data on the water vapor uncertainty profiles can clearly be seen in Fig  
406 2D, where all retrievals have the similar uncertainty above about 800 m where the DIAL data  
407 are being used. Including the DIAL data into the retrievals has a minor impact on the retrieved  
408 temperature profiles, as all three seem to agree a bit better qualitatively with the radiosonde  
409 above 1000 m (comparing Fig 2A with Fig 1A), and the  $1-\sigma$  uncertainties in temperature are  
410 slightly smaller (Fig 2C with Fig 1C).

#### 411 *4.2. Comparing mean uncertainty profiles*

412 While the case study above may be representative, the quality of a retrieval (i.e., its  
413 uncertainty and information content) is case specific. To provide a more complete picture of  
414 how the different passive-only and active+passive retrievals compare, we computed the mean  
415  $1-\sigma$  uncertainty profiles from all of the retrievals performed during Perdigao, as a wide range of  
416 environmental conditions (e.g., the surface temperature ranged from approximately 9 to 33 °C  
417 and the precipitable water vapor from 1.1 to 3.1 cm) were observed during the 5-week  
418 campaign. Figure 3 shows these mean uncertainty profiles for temperature (left) and water  
419 vapor (right) for the different passive-only (solid lines) and active+passive (broken lines), and  
420 Table 2 provides the mean values at 3 different heights.



421 Considering the passive-only retrievals, combining the AERI and MWR together has little  
422 impact on the resulting temperature retrieval in the lowest 3 km or on the water vapor retrieval  
423 below 1.5 km, compared to the AERI-only retrieval. However, the MWRz and MWRzo  
424 outperform the AERI for water vapor above 2 km. Most strikingly, the benefit of the passive  
425 retrieval synergy can be seen for water vapor above 1.5 km, where the improvement is up to  
426 30% compared to the single sensor retrievals. Adding the elevation scanning data to the MWR  
427 retrieval (i.e., the MWRzo vs MWRz) results in a smaller uncertainty in the temperature profile,  
428 especially below 400 m.

429 Including the nDIAL data into the retrievals greatly reduces the  $1-\sigma$  uncertainty in the water  
430 vapor profiles for all active+passive retrievals (relative to the passive-only results), and results  
431 in a slight decrease in the temperature uncertainty also. The AERI-based retrievals show  
432 smaller uncertainties than the MWR-based retrievals, with the exception in the water vapor  
433 retrievals above 2 km where the MWR-based retrieval has a smaller uncertainty than the AERI  
434 retrieval. The uncertainty in the AERI+nDIAL water vapor retrieval between 500 m and 2 km,  
435 where the nDIAL data are used, is slightly smaller than the uncertainty in the MWRz+nDIAL  
436 retrieval, suggesting that the AERI is adding more information to the DIAL observations than the  
437 MWR. However, above 2 km the combination of all sensors has distinguishably the best  
438 performance, indicating that all instruments are contributing to the sensor synergy. In  
439 quantitative numbers, the WVMR can be retrieved via sensor synergy with accuracies between  
440 0.4 and 0.6 g kg<sup>-1</sup> in the lowest 3 km, which between 1 and 2 km (the region where DIAL shows  
441 its optimal performance), is an uncertainty reduction of up to 50% compared to the passive  
442 retrieval synergy.

#### 443 4.3. Comparing mean cDFS profiles

444 The optimal estimation framework used in this study uses the *a priori* to help constrain the  
445 ill-posed retrieval, thereby allowing the algorithm to converge to a realistic solution more  
446 frequently. Looking at the DFS profile, especially when summed with altitude from the surface  
447 (called here the cumulative DFS profile), enables one to understand where the independent  
448 data in the observations are located vertically. Figure 4 shows the mean cumulative DFS  
449 profiles for the different retrievals; mean values at three specific heights are provided in Table  
450 3.

451 There are several important features in this figure. First, adding the elevation scanning data  
452 to the MWR retrieval (i.e., comparing the MWRz-only vs. MWRzo-only) increases the total DFS  
453 for temperature at 3 km by 0.4 (from 2.15 to 2.57), with almost all of this increase in the first  
454 500 m. [Note, however, that we have only used a single elevation angle to the MWRzo (Table  
455 1), and the inclusions of additional elevation angles would result in a slight increase the cDFS for  
456 temperature.] The AERI-only temperature retrieval has more information (3.87) in the lowest  
457 500 m than the MWRzo-only retrieval has in the lowest 3 km (2.57). Most of the information in  
458 the temperature retrievals is below 1.5 km, as the cDFS profiles become relatively constant  
459 above that level; this suggests that these passive-only and active+passive temperature  
460 retrievals will have limited ability to retrieve the structure of the temperature profile above  
461 that height.

462 The passive-only retrievals of water vapor show less total DFS (using the value at 3 km  
463 height) during Perdigoao relative to datasets at other field campaigns (e.g., Turner and Löhnert



464 2014; Blumberg et al. 2015). This is likely due to the spread in the covariance of the prior,  
465 because if the prior had (hypothetically) negligible spread then the derived information content  
466 from the observations would be vanishingly small. Nonetheless, we can still use this prior to  
467 demonstrate how the addition of the DIAL data to the retrievals changes the information  
468 content. The cDFS profiles for the water vapor retrievals clearly show the impact of including  
469 the nDIAL data above 500 m, as the cDFS profiles for the active+passive retrievals are markedly  
470 larger above that height than the passive-only retrievals (i.e., with values between 6 to 7  
471 compared to 2 to 3 at 3 km). The additional information on water vapor in the AERI below 500  
472 m relative to the MWR is clearly seen. However, the lidar does not always provide data to the  
473 same altitude and its noise levels can depend on atmospheric conditions (e.g., if there is a cloud  
474 above the lidar or not), and thus the spread in the cumulative DFS profiles was quite large (e.g.,  
475 from 2.0 to 9.4 for the MWRz+nDIAL at 3 km height; Table 3).

#### 476 *4.4. Impact of clouds*

477 One of the often-stated advantages of MWR-based retrievals, relative to infrared-based  
478 retrievals, is the ability to profile through clouds because the optical thickness of the cloud is  
479 markedly smaller in the microwave relative to the infrared for a given liquid water path (LWP).  
480 Figure 5 shows cDFS profiles from the MWRz-only and AERI-only temperature and water vapor  
481 retrievals during a 2h period when the sky transitioned from virtually clear sky to overcast.  
482 Three profiles with different LWP amounts (2, 10, and 60 g m<sup>-2</sup>, where the infrared is essentially  
483 opaque for the last – Turner 2007) are shown. The cloud base was at 1100 m and was assumed  
484 to be 100 m thick (there was no way to determine cloud top from other observations at the  
485 site). First, notice that as the cloud becomes optically thicker, the retrievals have more  
486 information about the temperature at cloud base. Second, the cloud becomes opaque in the  
487 infrared quickly, hence the cumulative DFS profile becomes essentially constant (especially for  
488 water vapor) above the cloud as the LWP values approach 60 g m<sup>-2</sup>. Meanwhile, the cloud is  
489 semi-transparent in the microwave for all LWP values, which is seen by the increasing cDFS  
490 profile (especially for water vapor) above the cloud. However, there is still only a small amount  
491 of information in the observations at heights above 1 km in the MWR (see left-hand panel of Fig  
492 4), and thus the increase in the information content in the MWR retrieval above the cloud is  
493 relatively limited.

494 The accurate understanding of where the information exists vertically is useful in order to  
495 properly assimilate these profiles into a numerical weather prediction model. There is often  
496 significant level-to-level correlation in the uncertainties of profiles retrieved from passive  
497 remote sensors (e.g., see Figure 10 of Turner and Blumberg 2019), and most data assimilation  
498 systems are not yet configured to handle correlated error in the observations. Coniglio et al.  
499 (2019) used the cDFS profile to identify the heights that should be assimilated to minimize the  
500 amount of correlated error from the retrieved profiles. Starting at a specified height (e.g., 50  
501 m), they identified heights where the cDFS had increased by 1 above that height, and this  
502 process continued until they either were unable to identify any other points or had reached the  
503 maximum height that they wanted to assimilate. This is illustrated by the dots on the profiles in  
504 Fig 5, with the first height taken at 50 m. For the AERI-retrieved profiles, three levels would be  
505 assimilated below the cloud with an additional level at cloud base or just above; the height of  
506 all of the temperature levels is pretty consistent for these three profiles. For the MWR, only



507 two levels would be assimilated due to the lower information content in the microwave  
508 observations, with the height of the second point changing dramatically due to how the cloud  
509 influences the vertical distribution of the DFS profile. Again, we remind the reader that the  
510 total DFS seen in this example is lower than that seen using this same retrieval framework in  
511 other field campaigns; we attribute this to the lack of spread in the *a priori* dataset used at  
512 Perdigao.

#### 513 4.5. Sensitivity to the nDIAL vs. vDIAL

514 The impact of adding any new observation depends partially on its error covariance matrix,  
515 as observations with larger uncertainties will add less information to the retrieved profile than  
516 observations with smaller uncertainties. For many lidars, coadding photon counting data in  
517 either time or altitude reduces the random errors, and thus would increase the information  
518 content and impact of using these lidar data in retrievals such as these. However, other  
519 features of the observations are also important. For example, during Perdigao, the lowest  
520 range gate that was considered useful from the nDIAL was at 500 m; data below that level  
521 suffered from systematic errors associated with the overlap function of the lidar (S. Spuler,  
522 personal communication). However, the vDIAL was designed to make good measurements at  
523 50 m above the surface, although generally speaking its maximum range is much less (order 1  
524 km; Newsom et al. 2020) than the nDIAL system (which frequently makes good water vapor  
525 measurements to altitudes well above 2 km). A natural question is how would the results  
526 already shown change if the vDIAL system was used instead of the nDIAL?

527 Unfortunately, this isn't straight-forward to answer as the vDIAL was not collocated with the  
528 other Perdigao instruments. Instead, we use the 6-week deployment of the vDIAL at the ARM  
529 SGP site (Newsom et al. 2020), which has an AERI with similar noise characteristics as the AERI  
530 deployed at Perdigao, as a surrogate. However, different *a priori* datasets were used for the  
531 retrievals at the two sites, which impacts the retrievals and hence the analysis. To help adjust  
532 for the contribution of the two priors, we performed AERI-only retrievals and AERI+vDIAL  
533 retrievals at the SGP so that we could look at the difference between the two, and compare  
534 that to the difference between the AERI-only and AERI+nDIAL retrievals at Perdigao (Figure 6).

535 The impact of the vDIAL data on the water vapor retrieval is most significant between 300  
536 and 1500 m and reaches relative values of up to 50% uncertainty reduction compared to the  
537 AERI-only retrieval. Above 1500 m, the AERI+vDIAL WVMR uncertainties increase quickly with  
538 height and approach the AERI-only uncertainties at 3 km. The AERI+nDIAL uncertainties are  
539 very similar to the AERI-only below 500 m (because the nDIAL data is not available at those  
540 levels), but are approximately 2x smaller than the AERI-only for all height between 500 m and 3  
541 km. Further, the change in the cDFS between 500 m and 3 km is larger for the nDIAL system  
542 relative to the vDIAL (Table 3). Thus, the ability of the nDIAL to see deeper into the troposphere  
543 than the vDIAL is clearly shown. Interestingly, the water vapor uncertainty in the AERI+vDIAL is  
544 smaller than the AERI+nDIAL in the 500 to 900 m range; however, this could easily be changed  
545 by adjusting how the DIAL data were coadded in the nDIAL (which had 1-min temporal  
546 resolution relative to the 20-min temporal resolution of the vDIAL – see Table 1).

547 Perhaps most noteworthy is the relative impact of the two DIALs on the retrieved  
548 temperature profile. The addition of the vDIAL data has almost no impact on the uncertainty or  
549 the cDFS profile relative to the AERI-only (Fig 6, Tables 2 and 3), whereas the nDIAL has a



550 marked impact on the retrieved temperature profile in the range from 500 m to 2.5 km with an  
551 reduction of the uncertainty of up to 0.25 K compared to the AERI-only retrieval. Here, the  
552 instrument synergy is obtained through a more exact determination of the water vapor profile  
553 by the nDIAL, which enables the AERI to reach a higher DFS value for temperature.

## 554 5. Conclusions

555 Many applications require profiles of temperature and humidity in the PBL. However, the  
556 accuracy and information content from different ground-based remote sensing instruments is  
557 not the same. Previous work (e.g., Löhnert et al. 2009; Blumberg et al. 2015) demonstrated  
558 that there is more information content in both temperature and water vapor from spectral  
559 infrared measurements (such as made by the AERI) than in spectral microwave radiometer  
560 measurements. These results depend strongly on the characteristics of the instrument systems  
561 being used; for example, if future generation MWRs are improved to have smaller random  
562 errors, then the information content in the observations would increase. The on-line python  
563 modules provided by Maahn et al. (2020) can be used to explore how the information content  
564 would change for different assumed random error levels in the MWR.

565 This study investigated the impact of ground-based sensor synergy for PBL thermodynamic  
566 profiling, and in particular, how the information content and random errors would change if an  
567 active remote sensor such as a water vapor DIAL was included into the retrieval. An open  
568 question going into this research was whether the inclusion of the water vapor DIAL  
569 observations with MWR radiance observations would have the same information content as  
570 retrievals that used the DIAL with the AERI observations. An important aspect of this study is  
571 that the same *a priori* data and retrieval framework were used for all of the different retrievals  
572 shown in this paper, which is crucial to truly quantify the differences as different retrieval  
573 frameworks can result in markedly different retrievals (Maahn et al. 2020). We have shown  
574 that including the DIAL data increases the water vapor information content and reduces water  
575 vapor errors in both the AERI+DIAL and MWR+DIAL retrievals, relative to the passive-only  
576 retrievals. However, the AERI+DIAL continues to have more information on water vapor than  
577 the MWR+DIAL. The best retrieval performance is observed when all three instruments are  
578 combined in one retrieval. Improvements are shown that decrease the uncertainty by 50%  
579 compared to passive-only retrievals between 1 and 2 km. At Perdigao, the AERI is shown to  
580 dominate retrieval accuracy in the lowest 500 m, from 500 m to 2 km it is the DIAL that  
581 primarily determines the accuracy, and above 2 km the three instruments complement each  
582 other optimally to obtain the best solution. Furthermore, the addition of the water vapor DIAL  
583 observations (slightly) improves the information content in temperature retrievals from the  
584 AERI+DIAL, but has no impact on the temperature profiles for the MWR+DIAL.

585 Passive ground-based remote sensors are relatively common, as these technologies are  
586 more mature, have been commercially available for several decades, and have been operated  
587 in networks (e.g., Caumont et al. 2016; Geerts et al. 2017; Yang and Min 2018). The recent  
588 advances in water vapor DIAL (e.g., Spuler et al. 2015; Newsom et al. 2020) are leading to the  
589 possibility that the two DIALs used in this study could be commercially available in the next  
590 several years, which is why they formed the focus of this study. There are other  
591 thermodynamic profiling active remote sensors that could be combined with MWRs and AERIS:



592 for example, Raman lidar and Radio Acoustic Sounding Systems (RASS). Studies have been  
593 conducted combining Raman lidar with both MWR data (e.g., Barrera-Verdejo et al 2016; Foth  
594 and Pospichal 2017) and AERI data (e.g., Turner and Blumberg 2019); however, these studies  
595 were in different environments using different *a priori* datasets, which makes quantitatively  
596 comparing their accuracy and information content problematic. There are currently efforts  
597 underway to evaluate the impact of RASS virtual temperature profiles observations on both  
598 AERI and MWR observations.

599 Sensor synergy does not have to just involve ground-based sensors. Ground-based MWR  
600 and AERI observations can also be combined with satellite observations to improve information  
601 content and accuracy, especially in the middle- and upper troposphere. Feltz et al. (2003)  
602 showed the impact on AERI retrievals and how these improved profiles could be used for  
603 evaluating thermodynamic structure near storms, while Ebell et al. (2013) performed a more  
604 classical information content study. Additional efforts (e.g., such as Toprov and Löhnert 2020)  
605 are needed, which show the impact of the high-temporal and high-spectral resolution  
606 geostationary infrared sounders with ground-based remote sensing systems and the impact on  
607 stability indices and other parameters.

608 It is possible that readers will consider this study as a suggestion about the optimal ground-  
609 based solution for thermodynamic profiling, especially for future operational networks. This  
610 paper provides insights into only one aspect of the cost-benefit solution (i.e., the relative  
611 differences of information content); considerations as to ease of use, durability and hardness,  
612 calibration stability, and other scientific traits (e.g., does the instrument provide information on  
613 macro- or microphysical cloud properties, aerosol properties, trace gases, etc.) also need to be  
614 considered.

615

## 616 Acknowledgments

617 This research was supported in part by the Department of Energy's Atmospheric System  
618 Research (ASR) program (DE-SC0014375 and 89243019SSC000034) and NOAA's Atmospheric  
619 Science for Renewable Energy program. We thank the groups that helped to collect the two  
620 primary datasets from the Perdigao field campaign in used in this paper: Petra Klein, Elizabeth  
621 Smith, Josh Gebauer, and Tyler Bell at the University of Oklahoma; and Scott Spuler, Matt  
622 Hayman, and Tammy Weckwerth at the National Center for Atmospheric Research.  
623 Additionally, we thank Raisa Lehtinen, Reijo Roininen, and Christoph Munkel at Vaisala and Rob  
624 Newsom at Pacific Northwest National Laboratory for the collection of the DIAL dataset at the  
625 SGP site. This article supports activities associated with COST (European Cooperation in Science  
626 and Technology) Action CA18235 "PROBE" (<http://www.probe-cost.eu>). We would like to  
627 thank Jason English for constructive comments on an earlier version of this manuscript. This  
628 paper does not imply endorsement for any particular instrument, nor reflect the views or  
629 official position of NOAA or the U.S. government.





## 630 References

- 631 Barrera-Verdejo, M., S. Crewell, U. Löhnert, E. Orlandi, and P. Di Girolamo, 2016: Ground-based  
632 lidar and microwave radiometry synergy for high vertical resolution absolute humidity  
633 profiling. *Atmos. Meas. Techniq.*, **9**, 4013-4028, doi:10.5194/amt-9-4013-2016.
- 634 Bluestein, H.B., Z.B. Wienhoff, D.D. Turner, D.W. Reif, J.C. Snyder, K.J. Thiem, and J.B. Houser,  
635 2017: A comparison of the fine-scale structures of a prefrontal wind-shift line and a  
636 strong cold front in the Southern Plains of the U.S. *Mon. Wea. Rev.*, **145**, 3307-3330,  
637 doi:10.1175/MWR-D-16-0403.1.
- 638 Blumberg, W.G., D.D. Tuner, U Löhnert, and S. Castleberry, 2015: Ground based temperature  
639 and humidity profiling using spectral infrared and microwave observations. Part II:  
640 Actual retrieval performance in clear-sky and cloudy conditions. *J. Appl. Meteor.*  
641 *Climatol.*, **54**, 2305 – 2319.
- 642 Caumont, O., D. Cimini, U. Löhnert, L. Alados-Arboledas, R. Bleisch, F. Buffa, M.E. Ferrario, A.  
643 Haefele, T. Huet, F. Madonna, and G. Pace, 2016: Assimilation of humidity and  
644 temperature observations retrieved from ground-based microwave radiometers into a  
645 convective-scale NWP model. *Q. J. Roy. Meteor. Soc.*, doi:10.1002/qj.2860.
- 646 Cimini, D., E. Campos, R. Ware, S. Albers, G. Giuliani, J. Oreamuno, P. Joe, S.E. Koch, S. Cober,  
647 and E. Westwater, 2011: Thermodynamic atmospheric profiling during the 2010 winter  
648 Olympics using ground-based microwave radiometry. *IEEE Trans. Geosci. Remote Sens.*,  
649 **49**, 4959-4969, doi:10.1109/TGRS.2011.2154337.
- 650 Cimini, D., M. Nelson, J. Güldner, and R. Ware, 2015: Forecast indices from a ground-based  
651 microwave radiometer for operational meteorology. *Atmos. Meas. Tech.*, **8**, 315-333,  
652 doi:10.5194/amt-8-315-2015.
- 653 Cimini, D., P.W. Rosenkranz, M.Y. Tretyakov, M.A. Koshelev, and F. Ramano, 2018: Uncertainty  
654 of atmospheric absorption model: Impact on ground-based radiometer simulations and  
655 retrievals. *Atmos. Chem. Phys.*, **18**, 15231-15259, doi:10.5194/acp-18-15231-2018.
- 656 Clough, S.A., M.W. Shephard, E.J. Mlawer, J.S. Delamere, M.J. Iacono, K. Cady-Pereira, S.  
657 Boukabara, and P.D. Brown, 2005: Atmospheric radiative transfer modeling: A summary  
658 of the AER codes. *J. Quant. Spectrosc. Radiative Trans.*, **91**, 233-244,  
659 doi:10.1016/j.jqsrt.2004.05.058.
- 660 Coniglio, M.C., G.S. Romine, D.D. Turner, and R.D. Torn, 2019: Impacts of targeted AERI and  
661 Doppler lidar wind retrievals on short-term forecasts of the initiation and early evolution  
662 of thunderstorms. *Month. Wea. Rev.*, **147**, 1149-1170, doi:10.1175/MWR-D-0351.1
- 663 Crewell, S., and U. Löhnert, 2007: Accuracy of boundary layer temperature profiles retrieved  
664 with multi-frequency, multi-angle microwave radiometry, *IEEE Trans. Geosci. Remote*  
665 *Sens.*, **45**(7), 2195–2201.
- 666 Dabberdt, W.F., and coauthors, 2005: Multifunction mesoscale observing networks. *Bull. Amer.*  
667 *Meteor. Soc.*, **86**, 961-982, doi:10.1175/BAMS-86-7-961.
- 668 De Angelis, F., D. Cimini, U. Löhnert, O. Caumont, A. Haefele, B. Pospichal, P. Martinet, F. Navas-  
669 Guzman, H. Klein-Baltink, J.-C. Dupont, and J. Hocking, 2017: Long-term observations minus  
670 background monitoring of ground-based brightness temperatures from a microwave  
671 radiometer network. *Atmos. Meas. Tech.*, **10**, 3947-3961, doi:10.5194/amt-10-3947-2017.



- 672 Degelia, S.K., X. Wang, and D.J. Stensrud, 2019: An evaluation of the impact of assimilating AERI  
673 retrievals, kinematic profilers, rawinsondes, and surface observations on a forecast of  
674 nocturnal convection initiation event during the PECAN field campaign. *Month. Wea.*  
675 *Rev.*, in press.
- 676 Ebell, K., E. Orlandi, A. Hünenbein, U. Löhnert, and S. Crewell, 2013: Combining ground-based  
677 with satellite-based measurements in the atmospheric state retrieval: Assessment of  
678 the information content, *J. Geophys. Res. Atmos.*, **118**, 6940–6956,  
679 doi:10.1002/jgrd.50548.
- 680 Feltz, W. F., W.L. Smith, H.B. Howell, R.O. Knuteson, H. Woolf, and H.E. Revercomb, 2003: Near-  
681 continuous profiling of temperature, moisture, and atmospheric stability using the  
682 Atmospheric Emitted Radiance Interferometer (AERI). *J. Appl. Meteor.*, **42**, 584-597.
- 683 Fernando, H.J., and 48 coauthors (including D.D. Turner), 2019: The Perdigao: Peering into  
684 microscale details of mountain winds. *Bull. Amer. Meteor. Soc.*, **100**, 799-819,  
685 doi:10.1175/BAMS-D-17-0227.1.
- 686 Foth, A., and B. Pospichal, 2017: Optimal estimation of water vapour profiles using a  
687 combination of Raman lidar and microwave radiometer. *Atmos. Meas. Tech.*, **10**, 3325-  
688 3344, doi:10.5194/amt-10-3325-2017.
- 689 Geerts, B., and coauthors, 2017: The 2015 Plains Elevated Convection At Night field project.  
690 *Bull. Amer. Meteor. Soc.*, **98**, 767 – 786.
- 691 Grasmick, C., B. Geerts, D.D. Turner, Z. Wang, and T.M. Weckwerth, 2018: The relation between  
692 nocturnal MCS evolution and its outflow boundaries in the stable boundary layer: An  
693 observational study of the 15 July 2015 MCS in PECAN. *Month. Wea. Review*, **146**, 3203-  
694 3226, doi:10.1175/MWR-D-18-0169.1
- 695 Hu, J., N. Yussouf, D.D. Turner, T.A. Jones, and X. Wang, 2019: Impact of ground-based remote  
696 sensing boundary layer observations on short-term probabilistic forecasts of a tornadic  
697 supercell event. *Wea. Forecasting*, **34**, 1453-1476, doi:10.1175/WAF-D-18-0200.1.
- 698 Johnson, A., X. Wang, K. Haghi, and D.B. Parsons, 2018: Evaluation of forecasts of a convectively  
699 generated bore using an intensively observed case study from PECAN. *Month. Wea.*  
700 *Rev.*, **146**, 3097-3122, doi:10.1175/MWR-D-18-0059.1
- 701 Knuteson, R. O., and coauthors, 2004a: Atmospheric Emitted Radiance Interferometer. Part I:  
702 Instrument design. *J. Atmos. Oceanic Technol.*, **21**, 1763-1776.
- 703 Knuteson, R. O., and coauthors, 2004b: Atmospheric Emitted Radiance Interferometer. Part II:  
704 Instrument performance. *J. Atmos. Oceanic Technol.*, **21**, 1777-1789.
- 705 Loveless, D.M., T.J. Wagner, D.D. Turner, S.A. Ackerman, and W.F. Feltz, 2019: A composite  
706 perspective on bore passages during the PECAN campaign. *Month. Wea. Rev.*, **147**,  
707 1395-1413, doi:10.1175/MWR-D-18-0291.1.
- 708 Löhnert, U., D.D. Turner, and S. Crewell, 2009: Ground-based temperature and humidity  
709 profiling using spectral infrared and microwave observations. Part 1: Simulated retrieval  
710 performance in clear sky conditions. *J. Appl. Meteor. Clim.*, **48**, 1017-1032,  
711 doi:10.1175/2008JAMC2060.1
- 712 Löhnert, U., and O. Maier, 2012: Operational profiling of temperature using ground-based  
713 microwave radiometry at Payerne: Prospects and challenges. *Atmos. Meas. Techniq.*, **5**,  
714 1121-1134, doi:10.5194/amt-5-1121-2012.



- 715 Maahn, M., D.D. Turner, U. Loehnert, D.J. Posselt, K. Ebell, G.G. Mace, and J.M. Comstock,  
716 2020: Retrievals and their uncertainties: What every atmospheric scientist should  
717 know. *Bull. Amer. Meteor. Soc.*, accepted.
- 718 Mlawer, E.J., and D.D. Turner, 2016: Spectral radiation measurements and analysis in the ARM  
719 program. *The Atmospheric Radiation Measurement Program: The First 20 Years*.  
720 Meteor. Monograph, 57, Amer. Meteor. Soc., 14.1-14.17,  
721 doi:10.1175/AMSMONOGRAPHIS-D-15-0027.1
- 722 Mueller, D., B. Geerts, Z. Wang, M. Deng, and C. Grasmick, 2017: Evolution and vertical  
723 structure of an undular bore observed on 20 June 2015 during PECAN. *Month. Wea.*  
724 *Rev.*, 145, 3375-3794, doi:10.1175/MWR-D-16-0305.1
- 725 National Research Council (NRC) Committee on Developing Mesoscale Meteorological  
726 Observational Capabilities to Meet Multiple National Needs, 2009: Observing Weather  
727 and Climate from the Ground Up: A Nationwide Network of Networks. National  
728 Academies Press, 234 pp.
- 729 Nehrir, A.R., K.S. Rapasky, and J.L. Carlsten, 2012: Micropulse water vapor differential  
730 absorption lidar: Transmitter design and performance. *Opt. Express*, 20, 137-151.
- 731 Newsom, R.K., D.D. Turner, R. Lehtinen, C. Muenkel, J. Kallio, and R. Roininen, 2020: Evaluation  
732 of a compact broadband differential absorption lidar for routine water vapor profiling in  
733 the atmospheric boundary layer. *J. Atmos. Oceanic Technol.*, 37, 47-65,  
734 doi:10.1175/JTECH-D-18-0102.1.
- 735 Payne, V.H., E.J. Mlawer, K.E. Cady-Pereira, and J.-L. Moncet, 2011: Water vapor continuum  
736 absorption in the microwave. *IEEE Trans. Geosci. Remote Sens.*, 49, 2194-2208,  
737 doi:10.1109/TGRS.2010.2091416.
- 738 Revercomb, H.E., H. Buijs, H.B. Howell, D.D. LaPorte, W.L. Smith, and L.A. Sromovsky, 1988:  
739 Radiometric calibration of IR Fourier transform spectrometers: Solution to a problem  
740 with the high-resolution interferometer sounder. *Appl. Opt.*, 27, 3210-3218.
- 741 Rodgers, C.D., 2000: *Inverse Methods for Atmospheric Sounding: Theory and Practice*. Series on  
742 Atmospheric, Oceanic, and Planetary Physics, Vol. 2, World Scientific, 238 pp.
- 743 Rose, T., S. Crewell, U. Löhnert, and C. Simmer, 2005: A network suitable microwave radiometer  
744 for operational monitoring of the cloudy atmosphere. *Atmos. Res.*, 75, 183-200,  
745 doi:10.1016/j.atmosres.2004.12.005.
- 746 Sica, R.J., and A. Haefele, 2016: Retrieval of water vapor mixing ratio from a multiple channel  
747 Raman-scatter lidar using an optimal estimation method. *Appl. Opt.*, 55, 763-777,  
748 doi:10.1364/AO.55.000763.
- 749 Sisterson, D.L., R.A. Peppler, T.S. Cress, P.J. Lamb, and D.D. Turner, 2016: The ARM Southern  
750 Great Plains (SGP) site. *The Atmospheric Radiation Measurement Program: The First 20*  
751 *Years*, Meteor. Monograph. Amer. Meteor. Soc. 57, 6.1-6.14,  
752 DOI:10.1175/AMSMONOGRAPHIS-D-16-0004.1.
- 753 Spuler, S. M., K.S. Repasky, B. Morley, D. Moen, M. Hayman, and A.R. Nehrir, 2015: Field-  
754 deployable diode-laser-based differential absorption lidar (DIAL) for profiling water  
755 vapor. *Atmos. Meas. Tech.* 8, 1073-1087, DOI:10.5194/AMT-8-1073-2015.
- 756 Toms, B.A., J.M. Tomaszewski, D.D. Turner, and S.E. Koch, 2017: Analysis of a lower-tropospheric  
757 gravity wave train using direct and remote sensing measurement systems. *Mon. Wea.*  
758 *Rev.*, 145, 2791-2812, doi:10.1175/MWR-D-0216.1.



- 759 Toporov, M., and U. Löhnert, 2020: Synergy of Satellite- and Ground-Based Observations for  
760 Continuous Monitoring of Atmospheric Stability, Liquid Water Path and Integrated  
761 Water Vapor, *J. Appl. Meteor. Climatol.*, early-online release,  
762 <https://doi.org/10.1175/JAMC-D-19-0169.1>
- 763 Turner, D.D., and J.E.M. Goldsmith, 1999: Twenty-Four-Hour Raman Lidar Water Vapor  
764 Measurements during the Atmospheric Radiation Measurement Program's 1996 and  
765 1997 Water Vapor Intensive Observation Periods. *J. Atmos. Oceanic Technol.* **16**, 1062-  
766 1076.
- 767 Turner, D.D., 2007: Improved ground-based liquid water path retrievals using a combined  
768 infrared and microwave approach. *J. Geophys. Res.*, **112**, D15204,  
769 doi:10.1029/2007JD008530
- 770 Turner, D.D., R.O. Knuteson, H.E. Revercomb, C. Lo, and R.G. Dedecker, 2006: Noise reduction  
771 of Atmospheric Emitted Radiance Interferometer (AERI) observations using principal  
772 component analysis. *J. Atmos. Oceanic Technol.*, **23**, 1223-1238
- 773 Turner, D. D., and U. Löhnert 2014: Information content and uncertainties in thermodynamic  
774 profiles and liquid cloud properties retrieved from the ground-based Atmospheric  
775 Emitted Radiance Interferometer (AERI). *J. Appl. Meteor. Climatol.*, **53**, 752-771,  
776 doi:10.1175/JAMC-D-13-0126.1.
- 777 Turner, D.D., V. Wulfmeyer, L.K. Berg, and J.H. Schween, 2014: Water vapor turbulence profiles  
778 in stationary continental convective mixed layers. *J. Geophys. Res.* **119**, 1-15,  
779 DOI:10.1002/2014JD022202.
- 780 Turner, D.D., E.J. Mlawer, and H.E. Revercomb, 2016a: Water vapor observations in the ARM  
781 program. *The Atmospheric Radiation Measurement Program: The First 20 Years*.  
782 Meteor. Monograph, 57, Amer. Meteor. Soc., 13.1-13.18,  
783 doi:10.1175/AMSMONOGRAPHS-D-15-0025.1
- 784 Turner, D.D., J.E.M. Goldsmith, and R.A. Ferrare, 2016b: Development and applications of the  
785 ARM Raman lidar. *The Atmospheric Radiation Measurement Program: The First 20*  
786 *Years*, Meteor. Monograph. Amer. Meteor. Soc. **57**, 18.1-18.15,  
787 DOI:10.1175/AMSMONOGRAPHS-D-15-0026.1.
- 788 Turner, D.D., and W.G. Blumberg, 2019: Improvements to the AERloe thermodynamic profile  
789 retrieval algorithm. *IEEE Selected Topics Appl. Earth Obs. Remote Sens.*, **12**, 1339-1354,  
790 doi:10.1109/JSTARS.2018.2874968.
- 791 Wagner, T. J., W. F. Feltz, and S. A. Ackerman, 2008: The temporal evolution of convective  
792 indices in storm-producing environments. *Wea. Forecasting*, **23**, 786 – 794.
- 793 Wagner, T.J., P.M. Klein, and D.D. Turner, 2019: A new generation of ground-based mobile  
794 platforms for active and passive profiling of the boundary layer. *Bull. Amer. Meteor.*  
795 *Soc.*, **100**, 137-153, doi:10.1175/BAMS-D-17-0165.1.
- 796 Weckwerth, T.M., K. Weber, D.D. Turner, and S.M. Spuler, 2016: Validation of a new water  
797 vapor micropulse differential absorption lidar (DIAL). *J. Atmos. Oceanic Technol.* **33**,  
798 2353-2372, DOI:10.1175/JTECH-D-16-0119.1.
- 799 Wulfmeyer, V., R.M. Hardesty, D.D. Turner, A. Behrendt, M. Cadetdu, P. Di Girolamo, P.  
800 Schluessel, J. van Baelen, and F. Zus, 2015: A review of the remote sensing of lower-  
801 tropospheric thermodynamic profiles and its indispensable role for the understanding



802           and simulation of water and energy cycles. *Rev. Geophys.*, **53**, 819-895,  
803           doi:10.1002/2014RG000476  
804    Yang, J., and Q. Min, 2018: Retrieval of atmospheric profiles in the New York State Mesonet  
805           using one-dimensional variational algorithm. *J. Geophys. Res.*, doi:  
806           10.1029/2018JD028272  
807  
808



809

810 **Table 1:**

811 Important specifications of the instruments used in this paper

Instrument	Specifications
MWR (HATPRO G4)	<ul style="list-style-type: none"> <li>• 7 frequencies between 22.2 and 31.4 GHz</li> <li>• 7 frequencies between 51.2 and 58.0 GHz</li> <li>• Off-zenith data collected at elevations of 18° and 162°</li> <li>• 1-s sky average, with elevation scans performed every 5 min; retrieval used single spectrum (both zenith and off-zenith) at desired time (e.g., close to sonde launch time)</li> <li>• Reference: Rose et al. 2005</li> </ul>
AERI	<ul style="list-style-type: none"> <li>• 324 wavenumbers in these intervals: 612-618, 624-660, 674-713, 713-722, 538-588, 860.1-864.0, 872.2-877.5, 898.2-905.4 cm<sup>-1</sup></li> <li>• 15-s sky average every 30-s; retrieval used single spectrum at desired time (e.g., close to sonde launch time)</li> <li>• Principal component noise filter used to reduce random error (Turner et al. 2006)</li> <li>• Reference: Knuteson et al. 2004 a,b</li> </ul>
nDIAL	<ul style="list-style-type: none"> <li>• Narrowband DIAL, transmitting at 830 nm</li> <li>• Temporal resolution: 1-min</li> <li>• Vertical resolution: 75-m</li> <li>• Minimum height: 500 m; Maximum height was approx. 3 km (typical)</li> <li>• Telescope receiver area (far field): 935 cm<sup>2</sup></li> <li>• Average transmitted pulse power: 5 μJ pulses at 9 kHz (45 mW)</li> <li>• Reference: Spuler et al. 2015; Weckwerth et al. 2016</li> </ul>
vDIAL	<ul style="list-style-type: none"> <li>• Broadband DIAL, transmitting at 911 nm</li> <li>• Temporal resolution: 20-min</li> <li>• Vertical resolution: variable from 100 m at 100 m AGL to 200 m at 1 km</li> <li>• Minimum height: 50 m; Maximum height was approx. 1 km (typical)</li> <li>• Telescope receiver area (far field): 615 cm<sup>2</sup></li> <li>• Average transmitted pulse power: 5.5 μJ pulses at 8 kHz (44 mW)</li> <li>• Reference: Newsom et al. 2020</li> </ul>

812

813

814



815

816 **Table 2:** Average uncertainty values (derived from  $S_{op}$ ) at three levels for temperature and  
 817 humidity for the different instrument combinations used in this study. The passive-only  
 818 retrievals are highlighted in gray, whereas the active+passive are in white. The values in  
 819 parentheses at 3 km show the 10<sup>th</sup> and 90<sup>th</sup> percentile at that height, thereby providing a  
 820 measure of the amount of variability in these statistics for each retrieval.

	Temperature Uncertainty [°C]			Water Vapor Uncertainty [g kg <sup>-1</sup> ]		
	500 m	1000 m	3000 m	500 m	1000 m	3000 m
MWRz-only	1.07	1.58	1.36 (1.34,1.36)	1.11	1.35	0.87 (0.83,0.87)
MWRzo-only	1.06	1.49	1.36 (1.34,1.36)	1.11	1.34	0.87 (0.82,0.87)
AERI-only	0.56	0.87	0.97 (0.86,1.22)	0.73	1.01	0.96 (0.82,1.07)
AERI+MWRz	0.56	0.86	0.94 (0.84,1.29)	0.69	0.97	0.71 (0.64,0.78)
MWRz+nDIAL	0.97	1.35	1.32 (1.28,1.35)	0.73	0.67	0.68 (0.47,0.85)
MWRzo+nDIAL	0.97	1.29	1.31 (1.27,1.35)	0.73	0.66	0.68 (0.46,0.84)
AERI+nDIAL	0.51	0.75	0.91 (0.81,1.22)	0.57	0.62	0.74 (0.49,1.05)
AERI+MWRz+nDIAL	0.51	0.75	0.91 (0.82,1.16)	0.55	0.61	0.60 (0.42,0.75)
AERI-only (SGP)	0.36	0.60	1.02 (0.82,1.41)	0.65	1.00	1.17 (0.90,1.45)
AERI+vDIAL (SGP)	0.35	0.57	1.01 (0.80,1.39)	0.39	0.68	1.10 (0.81,1.42)

821

822

823

824

825

826

827 **Table 3:** Average cDFS values at three levels for temperature and humidity for the different  
 828 instrument combinations used in this study. The passive-only retrievals are highlighted in gray,  
 829 whereas the active+passive are in white. The values in parentheses at 3 km show the 10<sup>th</sup> and  
 830 90<sup>th</sup> percentile at that height, thereby providing a measure of the amount of variability in these  
 831 statistics for each retrieval.

	Temperature cDFS value [unitless]			Water vapor cDFS value [unitless]		
	500 m	1000 m	3000 m	500 m	1000 m	3000 m
MWRz-only	1.51	1.82	2.15 (2.15,2.16)	0.94	1.14	1.92 (1.71,2.03)
MWRzo-only	1.85	2.22	2.57 (2.56,2.59)	0.94	1.13	1.92 (1.71,2.03)
AERI-only	3.87	4.55	5.50 (5.02,5.66)	1.45	1.83	2.70 (1.88,3.41)
AERI+MWRz	3.89	4.58	5.56 (5.15,5.66)	1.53	1.97	3.17 (2.70,3.81)
MWRz+nDIAL	1.51	1.82	2.16 (2.14,2.20)	1.11	2.62	6.23 (1.97,9.44)
MWRzo+nDIAL	1.84	2.20	2.57 (2.54,2.61)	1.10	2.61	6.22 (1.99,9.41)
AERI+nDIAL	3.87	4.52	5.48 (5.25,5.63)	1.67	3.25	7.00 (2.80,10.14)
AERI+MWRz+nDIAL	3.87	4.52	5.49 (5.25,5.63)	1.71	3.28	7.21 (3.21,10.15)
AERI-only (SGP)	4.80	5.53	6.58 (5.36,7.16)	1.72	2.08	2.97 (1.90,3.83)
AERI+vDIAL (SGP)	4.82	5.53	6.64 (5.45,7.13)	2.54	4.17	5.50 (2.42,8.40)

832

833

834



835 **Figures:**  
836

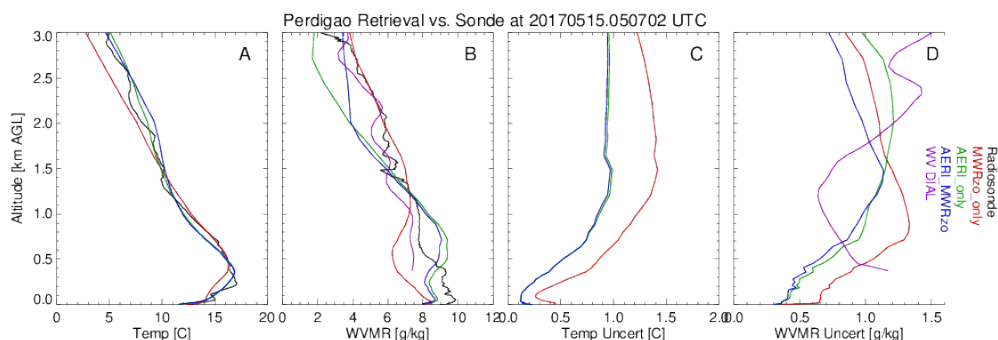


Fig 1: The retrieved profiles of temperature (A) and water vapor (B), with the uncertainties in these profiles (panels C and D, respectively), for the passive-only retrievals with the MWRzo only (red), AERI only (green), and AERI+MWRzo (blue) on 05:07 UTC on 15 May 2017 during Perdigao. The collocated radiosonde temperature and water vapor profiles are shown in black in (A) and (B), respectively. The water vapor observed by the DIAL and its uncertainty are included in the figure, although it is not used in any of these retrievals.

837  
838  
839  
840  
841  
842  
843

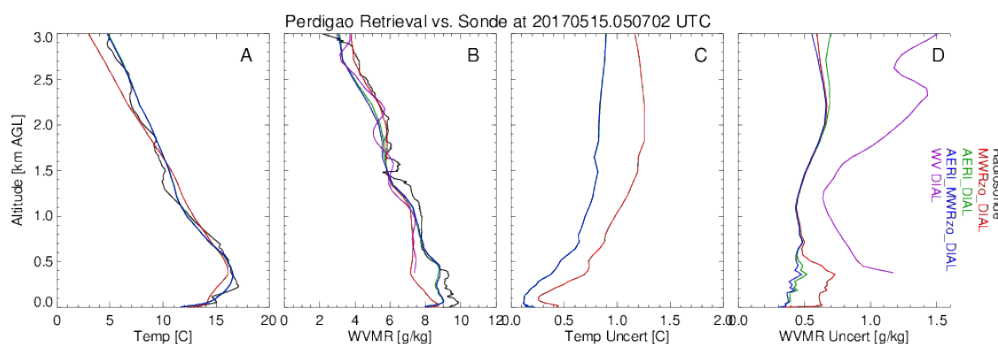


Fig 2: Same as Fig 1, except that the retrievals combine active and passive data with the MWRzo+DIAL (red), AERI+DIAL (green), and AERI+MWRzo+DIAL (blue). The water vapor observed by the DIAL and its uncertainty are included in the retrievals. See text for more details.

844  
845





846

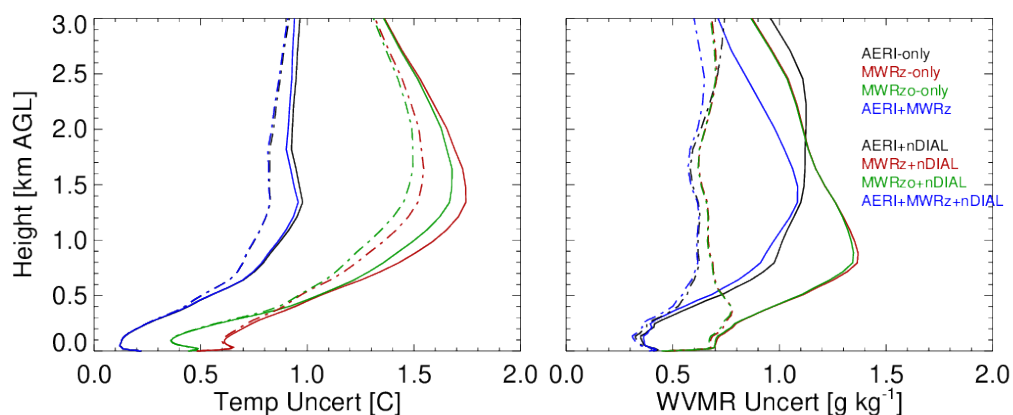


Fig 3: The mean uncertainty in temperature (left) and water vapor mixing ratio (right) for passive-only (solid lines) and active+passive (broken lines) retrievals during Perdigao.

847  
848  
849  
850  
851  
852  
853  
854

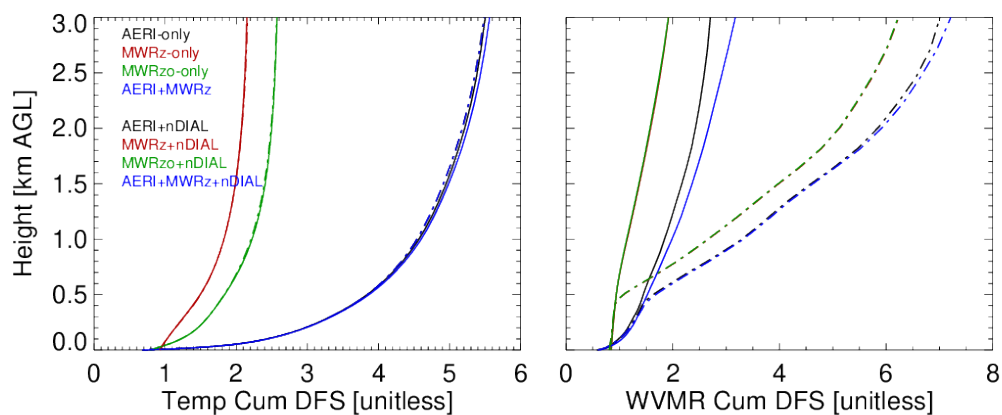


Fig 4: The mean cumulative degrees of DFS for temperature (left) and water vapor mixing ratio (right) for passive-only (solid lines) and active+passive (broken lines) retrievals during Perdigao. Note that the water vapor cumulative DFS profiles for MWRz and MWRzo retrievals are virtually identical (see Table 3) and hence overlap.

855



856

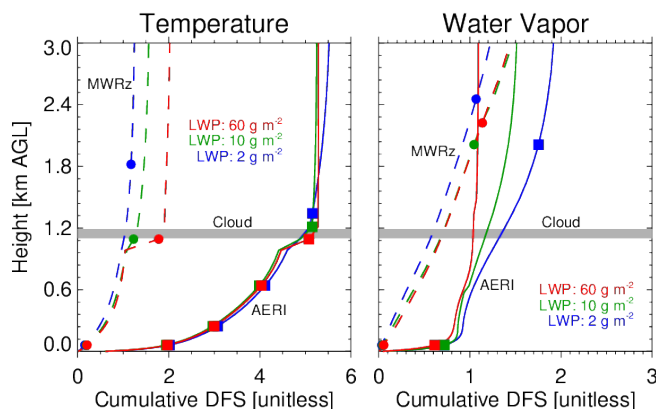


Fig 5: Profiles of cumulative degrees of freedom of signal from MWRz-only (dashed curves with dots) and AERI-only (solid curves with squares) temperature (left) and water vapor (right) retrievals for three samples between 03:00 and 05:00 UTC on 27 May 2017 during Perdigao. The different colors correspond to different LWP path values in the overhead cloud, whose height is indicated with the horizontal gray bar. The solid symbols indicate heights that would be assimilated, if the first level started at 50 m AGL and each level was separated by a unit of DFS. See the text for more details.

857

858

859

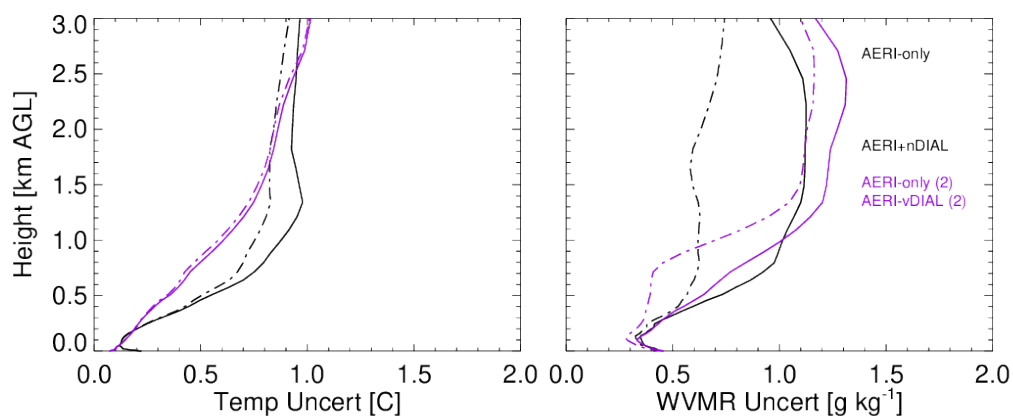


Fig 6: The mean uncertainty in temperature (left) and water vapor mixing ratio (right) for AERI-only (solid lines) and AERI+xDIAL (broken lines) retrievals during Perdigao (black) and SGP (purple), where the former used nDIAL data and the latter used vDIAL data. Note that different priors were used for the two locations; this impact is seen in the AERI-only retrievals as the noise levels of the two AERIs were similar.

860